CITRUS HUANGLONGBING DETECTION USING NARROW-BAND IMAGING AND POLARIZED ILLUMINATION

A. Pourreza, W. S. Lee, E. Raveh, R. Ehsani, E. Etxeberria

ABSTRACT. *The insect-spread bacterial infection known as citrus greening or Huanglongbing (HLB) is a very destructive citrus disease and has caused massive losses in Florida's citrus industry. Early, easy, and less expensive HLB detection based on particular symptoms, such as starch accumulation in the citrus leaf, would increase the chance of preventing the disease from being spread and causing more damage. The ability of narrow-band imaging and polarizing filters in detecting starch accumulation in symptomatic citrus leaf was evaluated in this study. A custom-made image acquisition system was developed for this purpose in which leaf samples were illuminated with polarized light using narrow-band high-power LEDs at 400 nm and 591 nm, and the reflectance was measured by two monochrome cameras. Two polarizing filters were mounted in perpendicular directions in front of the cameras so that each camera acquired an image with reflected light in only one direction (parallel or perpendicular to the illumination polarization). Four groups of textural features, including gray, local binary pattern, local similarity pattern, and gray-level co-occurrence features, were extracted and ranked using several feature selection methods. Seven classifiers (support vector machine, linear, naive Bayes linear, quadratic, naive Bayes quadratic, Mahalanobis, and k nearest neighbor) were evaluated, and the best classifiers and sets of features were selected based on their accuracy. The leaf samples were collected from the 'Hamlin' and 'Valencia' varieties of citrus. Three classes of samples (magnesium-deficient, HLB-positive zinc-deficient, and HLB-negative zinc-deficient) were considered in the classification process to confirm the starch detection ability of the system. Overall average accuracies of 93.1% and 89.6% in HLB detection were obtained for the 'Hamlin' and 'Valencia' varieties, respectively, using a step-by-step classification method. The results of this study showed that the starch accumulation in HLB-symptomatic leaves rotated the polarization planar of light at 591 nm, and this property can be effectively used in a fast and inexpensive HLB detection system.*

Keywords. *Classification, HLB, Image analysis, Starch concentration, Textural features.*

C itrus is the largest fruit crop in the state of Florida (Putnam, 2012). Based on 2012 statistics, more than 63% of the total U.S. citrus production is grown in Florida. The industry employs nearly 76,000 people directly or indirectly, and it generates almost $1 billion in tax revenues (Brown et al., 2011). One of the harshest diseases affecting citrus production is Huanglongbing (HLB), which is most likely caused by the insect-vectored α-protobacterium *Candidatus* Liberibacter asiaticus (Albrecht and Bowman, 2008). Yield reduction, decline in flavor quality, uneven color development, deformity, and eventual tree death are direct consequences of this disease. An overall 10% loss has been reported due to citrus fruit drop as a result of HLB disease (Choi et al., 2013). In Florida, HLB was first detected in 2005, and it has since spread to all of Florida's citrus-producing counties. Blotchy mottled leaves, lopsided fruits with inverted color, yellow shoots, and aborted seeds are some common symptoms of HLB (Gonzalez et al., 2012). To date, no effective treatment has been reported for this disease; however, early detection and removal of infected trees can help minimize the spread of the disease to other adjacent trees in the grove. Ground inspection of visual symptoms and polymerase chain reaction (qrt-PCR) tests are two common methods of HLB detection. Both methods are costly and time consuming.

Fast and easy methods of detection for plant diseases have improved farming productivity and prevented major losses in the agricultural industry. Machine vision is one of the most successful approaches in disease control and detection for both trees and herbaceous crops. Fluorescence, hyperspectral, and multispectral imaging, as well as infrared and nuclear magnetic resonance (NMR) imaging, are different machine vision-based methods that enable farmers to monitor their fields and effectively protect their products from diseases (Sankaran et al., 2010a).

Several vision-based methods have been tested for HLB detection. Mishra et al. (2007) reported that the wavelength regions including 530-564 nm (green peak), 710-715 nm (red edge), and two wavelengths (1041 nm and 2014 nm)

in the near-infrared region have the maximum discriminability between HLB-symptomatic and healthy trees. Kim et al. (2009) evaluated the ability of co-occurrence features extracted from color images of citrus leaf samples to classify the leaves in seven symptomatic classes including greening blotchy mottle, green islands, iron deficiency, magnesium deficiency, zinc deficiency, young flush leaves, and normal mature leaves. They employed stepwise discriminant analysis for feature selection and classification purposes. A classification accuracy of 86.7% was obtained when all classes were considered; however, the accuracy increased to 97.3% when the young flush and blotchy mottle classes were omitted from the classification procedure.

Mid-infrared spectroscopy has been employed by Sankaran et al. (2010b) to identify HLB infection in diseased, healthy, and nutrient-deficient citrus leaves. They showed that the spectral signature in the range of 5.15 to 10.72 μm, which was acquired from each ground sample, was capable of identifying HLB infection in leaves. An accuracy of over 90% in HLB detection was obtained using the k nearest neighbor (KNN) algorithm. In another study, Fourier transform infrared-attenuated total reflection (FT-IR-ATR) spectroscopy was employed to detect HLB-infected leaves. With this method, the leaf sample should be dried and ground before the analysis. The HLB status for 95% of 179 samples was correctly identified in this study (Hawkins et al., 2010).

Tree canopy reflectance measurements in four bands (570 nm and 670 nm in the visible range, and 870 nm and 970 nm in the near-infrared range) were determined to be capable of identifying HLB-symptomatic citrus trees. Mishra et al. (2011) calculated eleven different vegetation indices and used them in five classifiers: decision trees, KNN, logistic regression, neural network, and support vector machine (SVM). An accuracy of 97% was obtained for HLB detection using SVM and decision tree based classification algorithms. In a separate study, the authors noted that a single observation of the canopy spectral reflectance data in the range of 350 to 2500 nm was not sufficient to detect diseased trees; however, they achieved an HLB detection accuracy of >90% using multiple measurements and SVM or a weighted KNN classifier (Mishra et al., 2012).

Sankaran et al. (2011) extracted 86 spectral features in the visible and near-infrared range of 350 to 2500 nm with 25 nm intervals from citrus groves. The reduced number of features, including first derivatives, second derivatives, and a combined dataset, was acquired using principal component analysis (PCA) and used in several classifiers. The highest overall accuracy of 95% was obtained using the second derivatives dataset in a quadratic discriminant analysis (QDA) classifier. In another study, Sankaran and Ehsani (2011) evaluated the features of the same spectra including spectral reflectance and vegetation indices. They employed stepwise discriminant and regression analyses for feature selection and classifiers such as QDA and soft independent modeling of classification analogies (SIMCA) for citrus greening detection. They confirmed that using both types of features can result in classification accuracy higher than 80%.

Airborne multispectral and hyperspectral imaging methods have also been used in detection of HLB (Li et al., 2011; Li et al., 2012a; Li et al., 2012b; Li et al., 2013). These researchers determined that the reflectances of healthy and HLB canopies were different in both the visible and near-infrared (NIR) ranges. Their methods were able to detect most of the severely infected areas and achieved various accuracies ranging from 43% to 95% depending on the ground truthing accuracies and classifiers implemented. Additionally, laser-induced fluorescence imaging was considered as a potential tool for early citrus greening detection with a 95% confidence level (Pereira et al., 2011).

The overall objective of this study was to develop a sensing system based on machine vision that is capable of discriminating between HLB-symptomatic and healthy leaves using polarized light. This concept is based on the prominent starch accumulation that takes place in HLB-symptomatic leaves compared to the lack of starch in otherwise healthy leaves or those under any other biotic or abiotic stress. Additionally, the known capability of starch to rotate the polarization planar of polarized light (McMahon, 2004) was evaluated for HLB-symptomatic citrus leaves. The specific objectives were:

- To determine how starch accumulation in an HLB-symptomatic leaf affects the polarized light and how this can be used in HLB detection.
- To develop an imaging system that can highlight the starch accumulation in leaves under field conditions.
- To determine the best set of image features that differentiates HLB-symptomatic and healthy leaves.
- To evaluate the accuracy of the proposed method compared with other techniques such as qrt-PCR analysis, starch measurement, spectroscopy, and airborne imaging.

MATERIALS AND METHODS
PRELIMINARY EXPERIMENT
In order to evaluate the effect of starch accumulation in HLB-symptomatic leaves on the polarization planar of the light, an initial experiment was conducted in May 2010 in the Citrus Research and Education Center (CREC) in Lake Alfred, Florida. In this experiment, citrus canopies were illuminated (after sunset in darkness) with a halogen lamp (100 W, JCD type, GY 6.35) and a polarized filter mounted in front of the lamp. Leaf reflectance was measured using a portable spectrometer (HR-1024, Spectra Vista Corp., Poughkeepsie, N.Y.) with another polarized filter installed in front of the spectrometer in two separate positions: parallel to the lamp filter (to measure the maximum reflectance) and perpendicular to the lamp filter (to measure the minimum reflectance).

Figures 1a and 1b show maximum and minimum reflectance using parallel and perpendicular filters, respectively. The spectra are averages of ten different sample measurements, and their standard deviations are shown as error bars at each wavelength. Figure 1c is the minimum to maximum reflectance ratio of control (healthy) and greening (HLB-symptomatic) samples. The ratio of the healthy and symp-
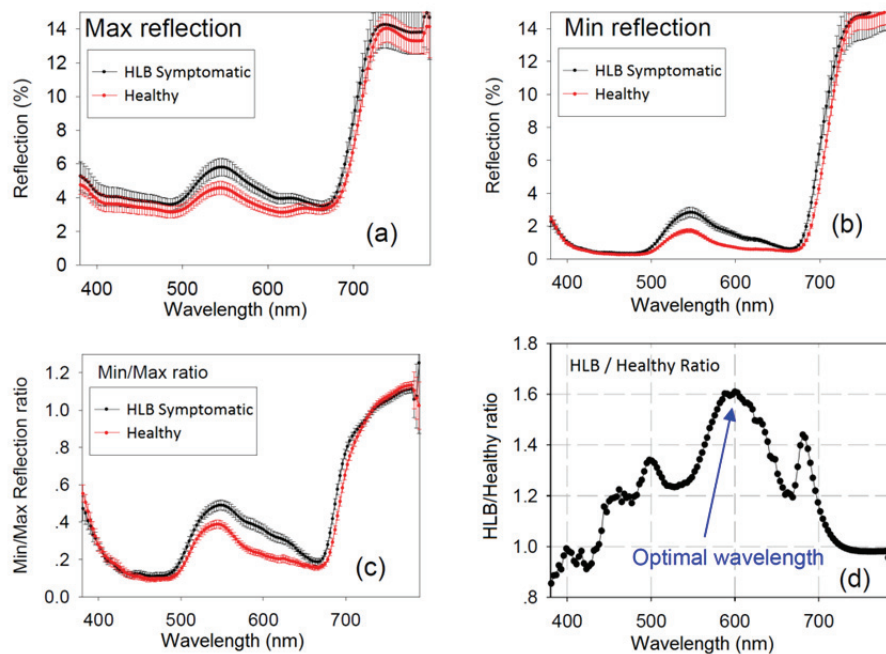
Figure 1. Detection of HLB-symptomatic canopy using diffuse reflectance in a citrus grove: (a) maximum reflectance, (b) minimum reflectance, (c) ratio of maximum and minimum reflectance, and (d) ratio of healthy leaf reflectance ratio and HLB-symptomatic leaf reflectance ratio.

tomatic leaf reflectance ratios is plotted in figure 1d. As shown in this figure, the highest ratio (1.6) was found near 600 nm, which suggests that this is the optimal wavelength for detecting HLB-symptomatic leaves. In addition, the ratio was close to 1.0 at 400 nm, which means that the min/max ratio of healthy and HLB-symptomatic leaves is the same, so this wavelength can be used as a reference wavelength.

ROTATION ANGLE OF POLARIZATION PLANAR AS CAUSED BY STARCH

In order to establish the degree to which pure starch rotates the polarization planar of the light, pure starch powder (cornstarch, Clabber Girl, Terre Haute, Ind.) was illuminated with polarized light, and its reflectance was measured using a spectrometer in the range of 400 to 1000 nm (USB2000+, Ocean Optics, Clearwater, Fla.). Based on the initial experimental results, the maximum rotation occurred at around 600 nm. Therefore, high luminous efficiency LEDs (LED Engin, San Jose, Cal.) at 591 nm (LZ1-00A100, 4 LEDs, 5 W per LED) were selected for illuminating the starch samples, since LEDs at exactly 600 nm were not available. A visible linear polarizing laminated film (Edmund Optics, Barrington, N.J.) was used for polarizing the light. One filter was mounted in front of the light source, and another was placed in front of the spectrometer sensor in the parallel direction. The angle between the spectrometer's filter and the light source's filter was then varied from 0° (parallel) to 90° (perpendicular) in 10° increments, and the reflectance was measured in each step. It was determined that the maximum reflectance of pure starch occurred when the light source's filter and the spectrometer's filter were exactly perpendicular to each other.

DATA COLLECTION

Two datasets were collected for this study. In each dataset, there were two main super classes: HLB-positive and HLB-negative. The HLB-positive super class included the HLB-symptomatic samples as well as the nutrient-deficient samples that also were HLB infected. The HLB-symptomatic class contained the samples whose HLB infection was confirmed by qrt-PCR test but that did not show any nutrient-deficiency symptoms. On the contrary, healthy samples and non-HLB-infected nutrient-deficient samples were included in the HLB-negative super class. The first dataset contained 90 citrus leaf samples ('Hamlin' sweet orange) in four classes, including healthy (32 samples), HLB-symptomatic (28 samples), HLB-negative zinc-deficient (15 samples), and HLB-positive zinc-deficient (15 samples) leaves, were collected from a grove located at the CREC in August 2012. The second dataset, which was collected from the same grove in December 2012, contained 96 citrus leaf samples ('Valencia') in five classes, including healthy (20 samples), HLB-symptomatic (20 samples), HLB-negative magnesium-deficient (20 samples), HLB-negative zinc-deficient (6 samples), and HLB-positive zinc-deficient (30 samples) leaves (Pourreza et al., 2013).

The concentration of starch in each leaf was measured in μg starch mm^{-2} according to the procedure described by Gonzalez et al. (2012). For this measurement, a tissue disk of 27.3 mm^2 from each leaf was excised with a paper puncher and homogenized in water. After a series of steps, including boiling, alcohol precipitation, and re-suspension of the starch in water, aliquots were combined with a 2% iodine solution. The absorbance was determined using a micro-plate reader (model 680, BioRad, Hercules, Cal.) at 595 nm. Starch concentration was calculated from an established standard curve. Finally, the threshold of 5 μg mm^{-2}

was used for HLB-infection detection (Gonzalez et al., 2012). For verification, a qrt-PCR analysis (Sankaran et al., 2010b) was also conducted in a diagnostic laboratory located at the U.S. Sugar Corporation's Southern Gardens processing plant in Clewiston, Florida, for each individual leaf to determine their infection status.

IMAGE ACQUISITION

Preliminarily evaluation showed that the accumulation of starch rotated part of the polarization planar of the light by 90° in a detectable magnitude. Based on this fact, an image acquisition system was designed to measure leaf reflection of the polarized light in both the parallel and perpendicular directions to the direction of the polarized illumination. In addition, 591 nm and 400 nm were selected for narrow-band illumination sources based on the preliminarily results, as described earlier.

Figure 2 shows a diagram of the image acquisition system for detecting HLB-symptomatic leaves. Two commercial monochrome cameras (EBC-B100G, EZ Spy Cam, Los Angeles, Cal.) with ICX404AL Sony CCD image sensors that had a horizontal resolution of 420 TV lines were used. The cameras were equipped with 25 mm narrow field of view lenses and were mounted at the top of the imaging box. A four-channel USB frame grabber (model 2255, Sensoray Co., Tigard, Ore.) was used to convert the analog output of the cameras to digital images with a resolution of 640×480 pixels.

A total of five high luminous efficiency LEDs (LED Engin, San Jose, Cal.), one at 400 nm (LZ1-00UA00, 5 W) and four at 591 nm (LZ1-00A100, 5 W), were mounted at the top of the imaging box for narrow-band illumination. Narrow field of view LED lenses were used to prevent any reflection inside the box. Two polarizing filters (visible linear polarizing laminated film, Edmund Optics, Barrington, N.J.) were also used: one in front of the illumination system and one of the cameras, and the other in front of the other camera in a perpendicular direction to the first filter. Therefore, at each wavelength, one camera acquired an image with reflected light that was in parallel polarization to the illumination polarization planar (maximum reflection), and the other camera acquired an image with reflected light that was in perpendicular polarization (minimum reflection). The imaging platform was enclosed in a wooden box (16 × 14 × 47 cm), so the LED light was the only source of illumination available for the sample images. An electronic circuit was designed to control the light intensity and switch between the two wavelengths. It also contained a 70 W LED driver (RCD-48-0.70-W, RECOM Electronic GmbH, Neu-Isenburg, Germany) that was designed for driving high-power LED applications. Therefore, the image acquisition system was able to produce images of each sample in four different conditions, i.e., using parallel and perpendicular filters at 400 nm and 591 nm illumination. The cameras' common field of view was determined by manual comparison of the images captured by the two cameras.

IMAGE PREPROCESSING

Commercial cameras are customarily equipped with automatic gain control (AGC), a feature that maintains similar image intensity and contrast regardless of the illumination conditions. In this study, the effect of AGC was removed using a calibration process because the real measurement of intensity was required. In order to solve this problem, calibration of images was conducted using the same background in all images. As the first step of this calibration, the average background gray levels in images captured with the
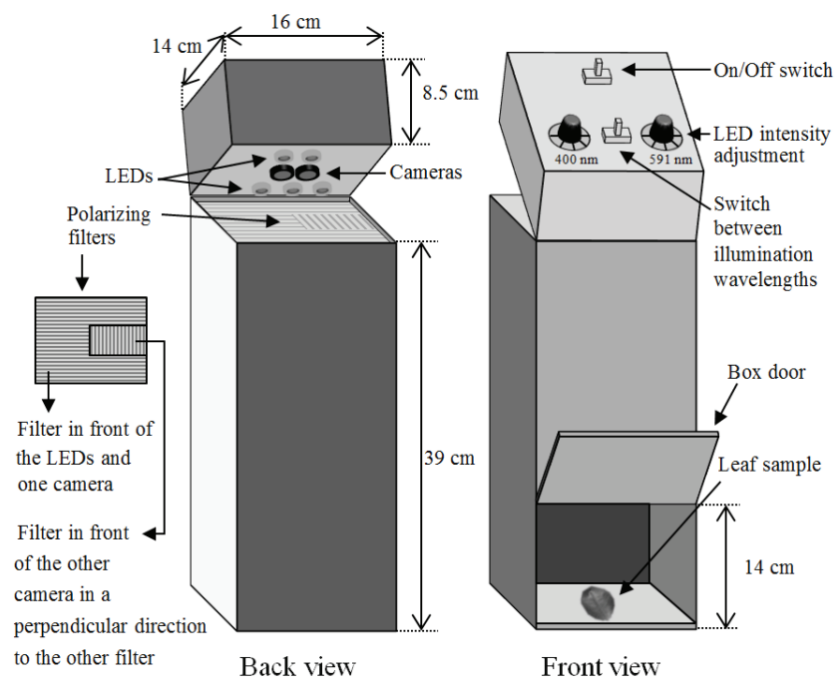

Figure 2. Image acquisition system for detecting HLB-symptomatic leaves. The top part of the imaging box can be opened to adjust the camera lenses and polarizing filters. The illumination intensity and wavelength can be adjusted at the top panel.

same illumination-polarization conditions was measured, and the ratio between this average to each image's background gray level was used as a unique gain multiplier for the corresponding image. As the second step, the exact reflectance of the background in all four illumination-polarization conditions was measured using a spectrometer, and the ratios between these values were used to adjust the intensity.

PIXEL-BASED ANALYSIS

All data analyses were conducted using MATLAB (ver. R2011a, The MathWorks, Natick, Mass.). Every pixel belonging to the leaf area in the images of all 90 samples (the 'Hamlin' dataset) was used in this analysis. Four monochrome images of each sample were acquired in four different illumination-polarization conditions:

- 400 nm (Max) image: acquired with the 400 nm LED and parallel polarizing filters mounted in front of the camera and the LED.
- 400 nm (Min) image: acquired with the 400 nm LED while the polarizing filter mounted in front of the camera was in a perpendicular direction to the polarizing filter mounted in front of the LED.
- 591 nm (Max) image: acquired with the 591 nm LEDs and parallel polarizing filters mounted in front of the camera and the LEDs.
- 591 nm (Min) image: acquired with the 591 nm LEDs while the polarizing filter mounted in front of the camera was in a perpendicular direction to the polarizing filter mounted in front of the LEDs.

"Max" represents the maximum reflectance, which was acquired using polarizing filters in parallel directions for the camera and the LEDs, and "Min" represents the minimum reflectance, which was acquired with polarizing filters in perpendicular directions for the camera and the LEDs. All four images were acquired of the same scene; therefore, there were four different values for each pixel, representing the reflectances for the four imaging conditions. In order to determine which imaging condition had the ability to differentiate the pixels belonging to the healthy and HLB-symptomatic areas, a k-means clustering method was conducted for each imaging condition separately. Therefore, k-means was applied to a one-dimensional feature vector at every iteration. As a result, it tried to determine the best gray-level threshold for image segmentation. Two clusters (healthy and HLB-symptomatic) were defined for the k-means algorithm, and the accuracy of correct clustering was evaluated and used to judge each imaging condition's ability in HLB detection. The clustering was performed in two runs: first, it was applied to the pixels belonging to all the images at the same time (general clustering); in the second run, it was applied to each image's pixels separately (individual clustering).

TEXTURAL FEATURE EXTRACTION

Textural features of the 591 nm (Min) images were used because the pixel-based analysis showed that only this imaging condition provided useful information for HLB detection (as explained later in the Results section). The fea-

tures were extracted from the leaf area in four different groups, including gray, local binary pattern (LBP), local similarity pattern (LSP), and gray-level co-occurrence matrix (GLCM) features.

LBP is a creative approach in image textural description in which each pixel in a 3×3 window is thresholded by the central gray level and replaced by 0 if its value is smaller than the central pixel value and by 1 if its value is larger than the central pixel value. The thresholded values are then considered an 8-bit binary value, and the equivalent decimal value replaces the central pixel value (Ojala et al., 1996). LSP uses almost the same principle of comparing the neighborhood pixels with the central pixel as used in LBP, but LSP uses a different approach. In LSP, a 2-bit code describes the relation between each neighbor pixel and the central pixel. A similarity range is defined in LSP, and if the neighbor pixel value is below, within, or above the similarity range, it is replaced by 00, 01, or 10, respectively. Each neighbor pixel code is multiplied by the corresponding weight, and the LSP code is created. The same approach used in LBP was also used in LSP to make it a rotational invariant. Both the LBP and LSP codes are rotated to obtain their minimum possible values, and this procedure makes them rotational invariants (Pourreza et al., 2011). The GLCM for an 8-bit gray-scale image is a 256×256 matrix that shows how often two different gray values are neighbors in four main directions (0°, 45°, 90°, and 135°). The normalized GLCM as described by Majumdar and Jayas (1999) was used in this research.

Table 1 lists the features extracted from normalized histograms ($p(i)$, where i is the gray level, which ranged from 0 to 255) in 591 nm (Min) images. These features are common statistical image descriptors that have been used frequently by other researchers. The first six features in table 1 (mean, standard deviation, third moment, smoothness, uniformity, and entropy) were also extracted from the normalized histograms of the LBP and LSP matrices (Pourreza et al., 2012). Table 2 lists equations used for extracting ten features from the normalized GLCM matrices ($g(i,j)$, where i and j are the indices of GLCM matrix elements) of 591 nm (Min) images.

Table 1. Features extracted from normalized histograms of gray, LBP, and LSP matrices.

Feature	Equation
Mean	$\mu = \sum_i i p(i)$
Standard deviation	$\sigma = \sqrt{\sum_i (i-\mu)^2 \, p(i)}$
Third moment	$\sum_i (i-\mu)^3 \, p(i)$
Smoothness	$1 - 1/(1+\sigma^2)$
Uniformity	$\sum_i p(i)^2$
Entropy	$-\sum_i p(i) \, log\{p(i)\}$
Maximum gray-level probability	$(i|\, p(i) = max)$
Range	$\{max\,(i|\,p(i) \neq 0) - min\,(i|\,p(i) \neq 0)\}$

**Table 2. Features extracted from normalized GLCM matrices.**

Feature	Equation
Mean	$\mu = \sum_{i,j} ig(i,j)$
Variance	$\sigma^2 = \sum_{i,j} (i-\mu)^2\, g(i,j)$
Entropy	$-\sum_{i,j} g(i,j)\, log\left\{g(i,j)\right\}$
Uniformity	$\sum_{i,j} \left\{g(i,j)\right\}^2$
Homogeneity	$\sum_{i,j} g(i,j)\, /\left\{1+(i-j)^2\right\}$
Inertia	$\sum_{i,j} (i-j)^2\, g(i,j)$
Cluster shade	$\sum_{i,j} (i+j-2\mu)^3\, g(i,j)$
Cluster prominence	$\sum_{i,j} (i+j-2\mu)^4\, g(i,j)$
Maximum probability	$max\left\{g(i,j)\right\}$
Correlation	$\sum_{i,j} (i-\mu)(j-\mu)\, /\, \sigma^2 g(i,j)$

CLASSIFICATION MODELS

Two principal component analysis (PCA) was performed on the feature vectors of both datasets, and all samples in each dataset were illustrated in separate two-dimensional plots in which the *x* and *y* axes were the first and second PCs. These plots show the distributions of samples that were used to design the step-by-step classification models. Figure 3 shows the classification model for the 'Hamlin' dataset, which was designed in three successive steps. In the first step, zinc-deficient samples were detected, followed by two HLB detections that were carried out separately as the second and third steps in the non-zinc-deficient class and the zinc-deficient class. Since there was an additional class of magnesium-deficient samples in the 'Valencia' dataset, the classification model was designed in four successive steps for this dataset (fig. 3). In the first step, the healthy and magnesium-deficient samples were detected from the rest of the dataset, and these two classes were divided in the second step. In the third step, the HLB-symptomatic samples were identified from the zinc-deficient samples, followed by another HLB detection conducted within the zinc-deficient class as the fourth step.

Gray, GLCM, LBP, and LSP features were investigated and ranked both separately and together. The "rankfeatures" function of MATLAB was used to rank the features that contribute more in each step of the classification. In this method, a nonlinear matrix equation under an orthonormal coordinate system was solved, and the optimal transformation matrix solution was determined from the nonlinear matrix equation using a recursive algorithm (Xuan et al., 1996). The performance of seven supervised learning methods, including support vector machine (SVM), linear, naive Bayes linear, quadratic, naive Bayes quadratic, Mahalanobis, and KNN, were evaluated using MATLAB functions. SVM tries to minimize the misclassification error by constructing a hyperplane that maximizes the margin between the two classes' nearest training data points. The linear method tries to project all the data points to a one-dimensional space and classify them based on the training set. The quadratic classifier is similar to the linear classifier with the assumption of normally distributed features in each class; however, each class's covariance is not necessarily identical. The naive Bayes classifiers add an assumption (to the linear and quadratic classifiers) in which the existence of a specific descriptor in a class is not related to the existence of any other descriptor. The Mahalanobis classifier works based on the general squared interpoint distance (or Mahalanobis distance) between data points of the classes. The KNN method also classifies samples based on the closest training examples' label (Bishop, 2006). A *k*-fold (five-fold) cross-validation method (Huang and Chang, 2007) was employed in all classification steps to confirm that the achieved results were independent of the training and validation sets. The dataset was randomly divided into five folds (four folds for training and one fold for validation) in each classification, and the whole process was repeated ten times. Then the range and average accuracy were determined and considered for the system evaluation. In order to find the optimized number of features in each step, each classifier was employed several times using different numbers of top features (starting with one feature) until the accuracy reached its highest level. The classifier that achieved the highest accuracy with the minimum number of features was considered the best classifier in the corresponding step.
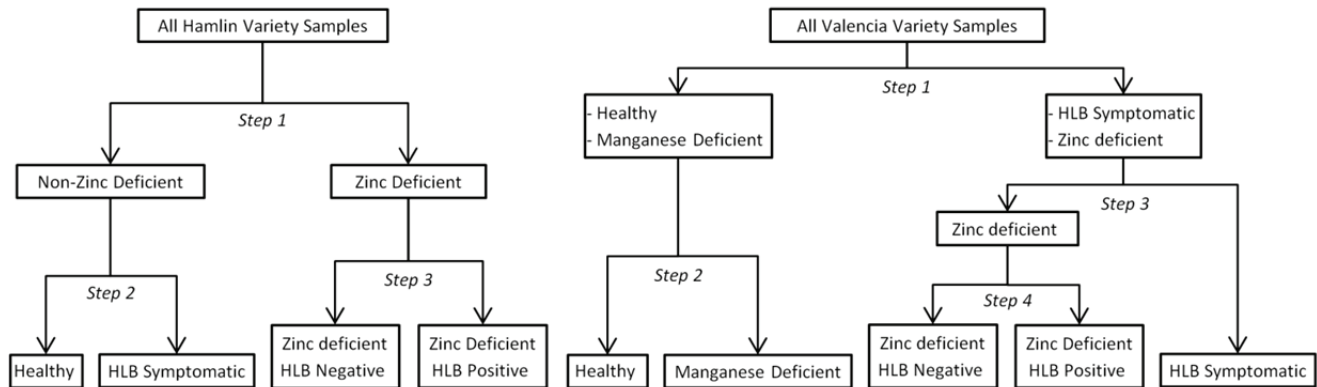
Figure 3. Step-by-step classification models for the 'Hamlin' (left) and 'Valencia' (right) datasets.

After determining the best combination of features and classifier for all the steps, each dataset was divided randomly into two equal sets. The whole model was then conducted with one set was used as the training set and the other set used as the validation set. Afterward, the classification model was repeated with the two sets in exchanged roles. Therefore, classification results for all samples were obtained.

RESULTS

IMAGE PREPROCESSING

Figure 4 shows examples of leaves representing each class in both datasets. Healthy samples were mostly evenly green in color, while HLB-symptomatic, magnesium-deficient, and zinc-deficient leaves had some similar yellow molting patterns. The molting symptoms on HLB-symptomatic samples were in a range of very clear symptoms (for advanced levels of infection) to unclear symptoms (for early stages of infection). Additionally, HLB symptoms were typically in an asymmetric pattern, while zinc and magnesium deficient leaves usually had a symmetric pattern of molting; nevertheless, they were not easily distinguishable. HLB infection in a zinc-deficient leaf was even more difficult to detect, since the zinc symptoms masked HLB symptoms.

Figure 5 shows example images of two leaves (one healthy and one HLB-symptomatic) before and after the calibration. The average intensity usually decreased after calibration of the images that were acquired using perpendicular filters, i.e., the 400 nm (Min) and 591 nm (Min) images. The effect of AGC was mostly cancelled using the

proposed gain adjustment method. Although the original reflectance was not completely recovered using this method, the correct reflectance ratios between two polarization conditions in each wavelength were retrieved, which was acceptable for this study.

STARCH MEASUREMENT AND qrt-PCR ANALYSIS

In a qrt-PCR analysis, a positive reaction is identified by the accumulation of a fluorescent signal. The cycle threshold (CT value) is the number of cycles necessary for the fluorescent signal to cross the threshold. A CT threshold of 33 was selected to indicate HLB infection, as is customary for state labs (Li et al., 2006). CT values below this threshold indicated HLB infection of the samples. Tables 3 and 4 show the results of the qrt-PCR analysis by the CT values for each sample as well as the corresponding starch concentrations for the 'Hamlin' and 'Valencia' datasets, respectively. The CT values in the healthy, magnesium-deficient, and zinc-deficient HLB-negative classes were above the threshold; therefore, they were considered HLB-negative samples. Contrarily, the CT values in the HLB-symptomatic and zinc-deficient HLB-positive classes were below the established threshold value. Based on these results, the 'Hamlin' dataset included 32 healthy, 28 HLB-symptomatic, 15 zinc-deficient HLB-negative, and 15 zinc-deficient HLB-positive samples. The 'Valencia' dataset included 20 healthy, 20 HLB-symptomatic, 20 magnesium-deficient, 6 zinc-deficient HLB-negative, and 30 zinc-deficient HLB-positive samples.

PIXEL-BASED ANALYSIS

Figure 6 shows some examples of images acquired using
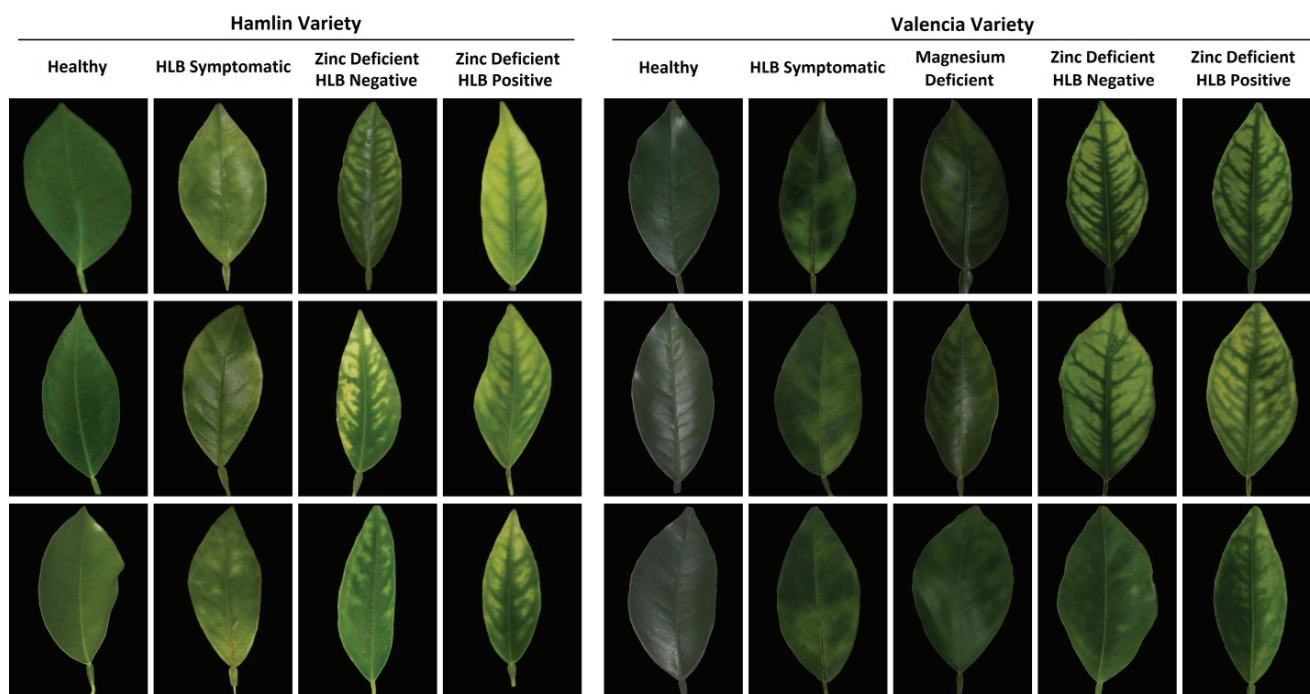
Figure 4. Images of leaves in four classes for the 'Hamlin' dataset (left) and in five classes for the 'Valencia' dataset (right) used for HLB analyses. Three samples are presented for each category to demonstrate the variability for each condition and the frequent overlapping of characteristics. Magnesium-deficient leaves were the most difficult to differentiate from HLB-symptomatic leaves. HLB infection within the zinc-deficient class was also impossible to identify by eye.

Figure 5. Example of calibration results for two 'Hamlin' leaves: (top) healthy sample and (bottom) HLB-symptomatic sample.

Table 3. Results of qrt-PCR analysis and starch measurement for the 'Hamlin' dataset.

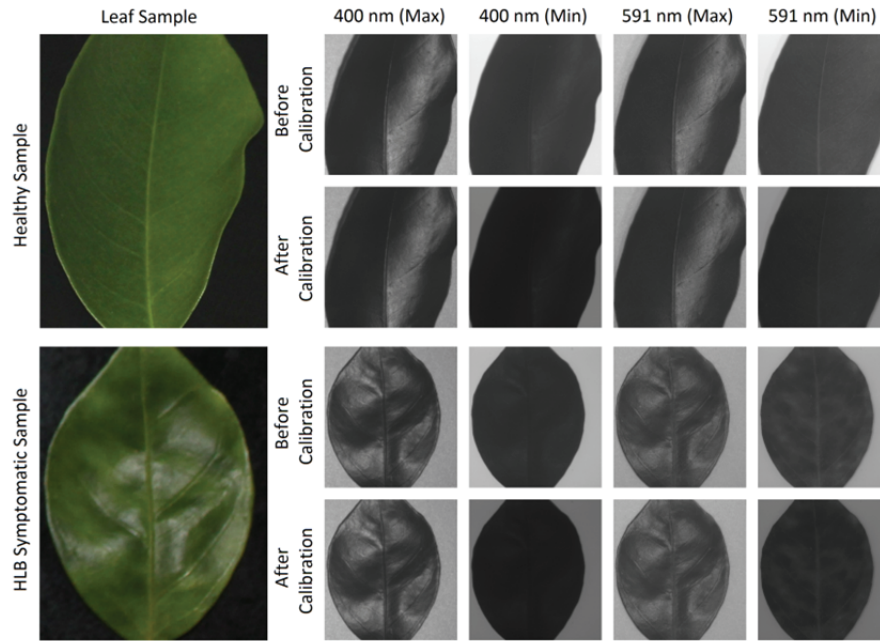|	Healthy			HLB-Symptomatic			Zinc-Deficient HLB-Negative			Zinc-Deficient HLB-Positive	
Sample No.	qrt-PCR (CT)	Starch (μg mm^{-2})	Sample No.	qrt-PCR (CT)	Starch (μg mm^{-2})	Sample No.	qrt-PCR (CT)	Starch (μg mm^{-2})	Sample No.	qrt-PCR (CT)	Starch (μg mm^{-2})
1	40	1.46	33	31.98	20.02	61	40	7.65	76	24.6	18.47
2	40	2.13	34	30.99	25.19	62	40	7.44	77	24.11	57.01
3	40	1.91	35	27.36	10.79	63	40	8.04	78	23.97	58.99
4	40	1.07	36	26.09	12.49	64	40	12.41	79	23.81	17.51
5	40	2.10	37	22.93	29.26	65	40	5.60	80	23.7	17.37
6	40	3.16	38	22.92	8.35	66	40	9.11	81	23.51	2.58
7	40	1.77	39	22.81	46.62	67	39.78	7.27	82	23.38	21.72
8	40	2.58	40	22.54	61.24	68	39.46	2.63	83	23.19	8.99
9	40	3.47	41	22.49	82.32	69	39.32	14.81	84	22.62	9.42
10	40	1.31	42	22.46	5.12	70	38.83	18.13	85	22.53	43.15
11	40	2.03	43	22.43	11.94	71	37.93	11.55	86	22.23	41.48
12	40	1.48	44	22.34	61.77	72	37.18	4.04	87	21.76	45.98
13	40	0.86	45	22.17	82.32	73	36.86	10.67	88	21.61	74.11
14	40	1.79	46	22.08	71.24	74	36.78	28.06	89	21.47	82.32
15	40	2.51	47	22.07	51.43	75	36.24	2.63	90	21.21	9.95
16	40	0.79	48	22.05	60.04						
17	40	2.01	49	21.86	39.28						
18	40	1.07	50	21.45	54.90						
19	40	1.67	51	21.45	43.66						
20	40	1.24	52	21.37	72.75						
21	40	0.93	53	21.35	61.86						
22	40	0.91	54	21.31	11.38						
23	40	2.29	55	21.27	70.86						
24	40	1.05	56	21.11	82.32						
25	40	1.17	57	21.11	38.54						
26	40	1.77	58	20.86	69.28						
27	39.84	2.37	59	20.76	82.32						
28	37.30	0.55	60	20.7	65.02						
29	36.51	2.25									
30	36.00	1.53									
31	34.91	2.44									
32	33.53	21.72									

the image acquisition system, including healthy, HLB-symptomatic, zinc-deficient HLB-negative, and zinc-deficient HLB-positive leaves from the 'Hamlin' dataset. The first column shows each sample's color image, and the following four columns show the same sample images in four different imaging conditions.

An example of image segmentation based on general clustering (a single threshold for all images) in which the k-means algorithm was applied once to all the samples at the same time is shown in figure 7. The investigation established that the 400 nm (Max) images did not contain any

Table 4. Results of qrt-PCR analysis (CT values) and starch measurement (μg mm^{-2}) for the 'Valencia' dataset.

Healthy			x	HLB-Symptomatic			x	Magnesium-Deficient			x	Zinc-Deficient HLB-Negative			x	Zinc-Deficient HLB-Positive		
Sample	qrt-PCR	Starch		Sample	qrt-PCR	Starch		Sample	qrt-PCR	Starch		Sample	qrt-PCR	Starch		Sample	qrt-PCR	Starch
1	40	1.56		21	23.38	24.35		41	40	0.42		61	36.71	11.36		77	23.42	23.66
2	40	1.61		22	23.14	44.12		42	40	0.57		62	37.37	20.90		78	22.56	4.36
3	40	0.77		23	21.12	22.71		43	40	0.52		63	40	27.00		79	23.78	0.69
4	40	0.74		24	22.35	43.05		44	40	0.52		64	40	11.13		80	23.38	13.02
5	40	1.11		25	22.64	44.74		45	40	0.69		65	37.89	40.30		81	21.69	29.78
6	40	1.96		26	21.61	20.85		46	40	1.31		66	36	12.79		82	21.35	51.53
7	38	1.73		27	23.33	68.99		47	40	1.14						83	22.18	8.60
8	40	1.66		28	22.39	44.02		48	40	1.04		Zinc-Deficient HLB-Positive				84	25.6	18.25
9	40	3.37		29	22.06	42.98		49	40	1.44						85	26.93	2.08
10	40	0.39		30	23.39	38.83		50	37.48	0.54		Sample	qrt-PCR	Starch		86	22.51	40.07
11	38.85	1.93		31	21.07	32.09		51	40	0.69		67	22.9	47.12		87	22.41	47.81
12	40	1.41		32	23.26	42.65		52	39.31	0.84		68	21.33	55.87		88	23.03	67.78
13	40	1.46		33	24.34	5.68		53	40	0.62		69	21.41	10.69		89	21.25	19.66
14	40	0.87		34	24.9	24.20		54	40	0.92		70	23.16	22.81		90	23.31	30.35
15	40	1.31		35	23.39	34.47		55	40	0.72		71	23.35	39.50		91	25.67	22.74
16	40	1.04		36	22.98	51.38		56	40	0.52		72	21.17	29.83		92	25.34	50.81
17	40	0.94		37	22.22	54.11		57	40	0.27		73	22.54	14.51		93	23.05	35.02
18	40	1.29		38	22.81	41.96		58	40	1.58		74	22.29	36.92		94	20.56	45.08
19	40	2.58		39	23.9	26.78		59	40	0.92		75	21.64	49.03		95	29.24	3.94
20	40	1.78		40	22.2	41.29		60	40	0.30		76	27.57	27.38		96	24.74	42.48
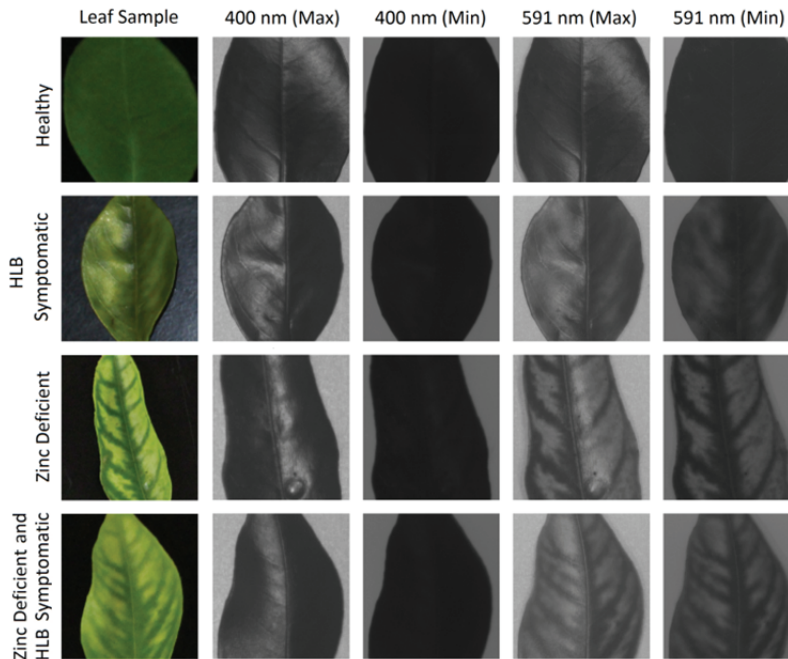
Figure 6. Images acquired using the image acquisition system with four imaging conditions ('Hamlin' dataset).

useful information about the symptomatic areas, and the clustering procedure only distinguished the glossy (high intensity) parts of the leaf from the non-glossy (low intensity) parts. The pixel values belonging to healthy and HLB-symptomatic (or zinc-deficient) areas were also not significantly different in the 400 nm (Min) images, as expected based on the preliminarily results. In the 591 nm (Max) images, the pixel values belonging to healthy, HLB-symptomatic, and zinc-deficient areas were different; however, there were also some glossy parts on the leaves (especially on healthy leaves) in which the pixel values were extremely similar to non-healthy parts, such as HLB-symptomatic and/or zinc-deficient parts. However, the 591 nm (Min) images contained very useful information, and the non-healthy parts were distinctive, as shown in figure 7.

Due to the incomplete cancelation of the AGC effect, the overall average intensity of the image for some samples was different from that of others in the 591 nm (Min) images. This led to a misclassification of some healthy pixels into non-healthy classes, including HLB-symptomatic or zinc-deficient classes; however, the healthy and non-healthy areas were distinguishable when the clustering was performed for individual samples separately. Figure 8 shows two examples of segmentation based on general and individual clustering. The top sample in figure 8 is an HLB-symptomatic sample in which the image intensity was below the average, so the general clustering segmented most of its pixels into a healthy cluster (green color), while the individual clustering (individual threshold for each image) was able to detect the symptomatic areas more accu-
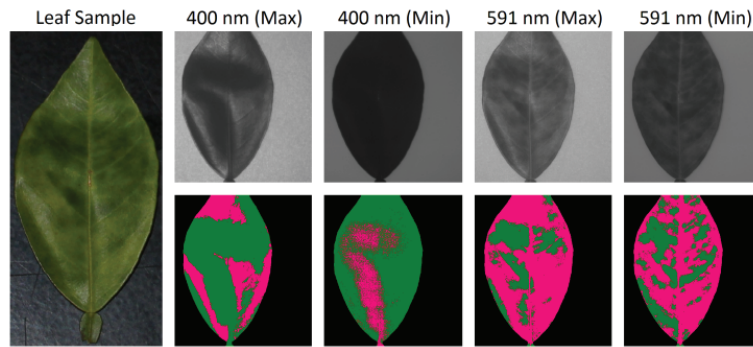
Figure 7. Example of image segmentation based on general clustering using *k*-means for an HLB-symptomatic sample. Green and pink colors indicate healthy and symptomatic clusters, respectively ('Hamlin' dataset).
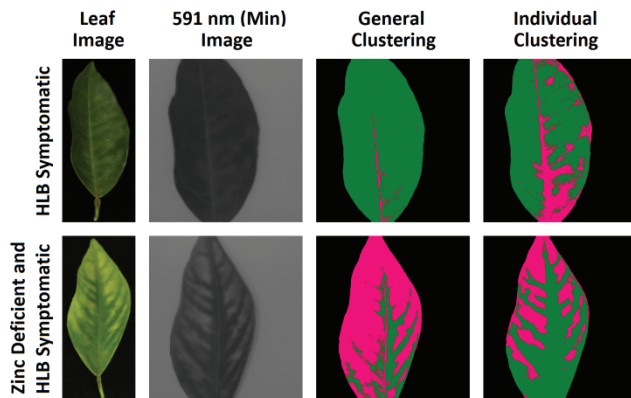

Figure 8. Comparison of the results of two segmentation methods based on general and individual clustering for an HLB-symptomatic leaf (above) and a zinc-deficient HLB-positive leaf (below). Green and pink colors indicate healthy and symptomatic clusters, respectively ('Hamlin' dataset).

rately. The opposite situation happened for the bottom sample in figure 8, in which the image intensity was higher than the average and the general clustering misclassified many healthy pixels into a symptomatic cluster. The individual clustering was able to more accurately distinguish the healthy and symptomatic areas in this case as well. From these data, it was concluded that employing the pixel values alone did not result in a general criteria with high recognition accuracy; however, some features, such as textural features, that describe each sample individually could play a more effective role in the classification process.

STEP-BY-STEP CLASSIFICATION

Table 5 lists the best set of features and classifier that resulted in the maximum average accuracy in each step of the classification models. The Mahalanobis classifier presented the best performance in all three classification steps for the 'Hamlin' dataset and in the first classification step for the 'Valencia' dataset.

Table 6 lists the best sets of features that were employed in the classification steps. Zinc deficiency in the 'Hamlin' dataset was detected with an average accuracy of 97.5% using the top 15 features of all feature groups. The healthy samples were identified with 100% accuracy using the 14 top features, while the highest HLB identification rate was 92.9%. The zinc-deficient HLB-negative samples were also identified with 100% accuracy using only the top three features, which were from the LBP feature group, while the highest HLB detection within the zinc-deficient class was 80%. Healthy and magnesium-deficient samples were identified with an accuracy of 100.0% at the first and second steps of the classification model using the Mahalanobis (with the top 13 features) and SVM (with the top two features) classifiers, respectively. The HLB-symptomatic samples were also recognized from zinc-deficient samples using the linear classifier and the top six features, with an average accuracy of 94.5% at the third step of the classification model. The best average classification rate (83.3%) for HLB identification within the zinc-deficient class was obtained using the linear classifier and the top four features.

Using the best set of features and classifier for each step, complete classification models were performed for all samples in each dataset. Tables 7 and 8 illustrate the step-by-step classification results for the 'Hamlin' and 'Valencia'

Table 5. The best set of features and classifier for each step of the classification models.[a]

Step No.	Step Description	TPR (%)	FPR (%)	Best Classifier	No. of Top Features
'Hamlin' dataset					
1	Identification of zinc-deficient samples from rest of dataset.	96.7	1.7	Mahalanobis	15
2	Identification of HLB-positive samples within non-zinc-deficient class.	92.9	0.0	Mahalanobis	14
3	Identification of HLB-positive samples within zinc-deficient class.	80.0	0.0	Mahalanobis	3
'Valencia' dataset					
1	Identification of healthy and magnesium-deficient samples from rest of dataset.	100.0	0.0	Mahalanobis	13
2	Identification of healthy samples from magnesium-deficient samples.	100.0	0.0	SVM	2
3	Identification of HLB-symptomatic samples from zinc-deficient samples.	88.9	0.0	Linear	6
4	Identification of zinc-deficient HLB-positive samples from zinc-deficient HLB-negative samples.	83.3	16.7	Linear	4

[a] TPR = true positive rate, and FPR = false positive rate.

Table 6. Sets of features used in the step-by-step classification models. The features in each step were ordered based on their ranking, which indicates the contribution level of each feature to an accurate classification process.

Step	Features
'Hamlin' dataset	
1	LBP entropy, Gray smoothness, LSP uniformity, LBP standard deviation, GLCM cluster shade, GLCM maximum probability, LSP third moment, LBP mean, LSP smoothness, Gray mean, Gray entropy, GLCM correlation, Gray standard deviation, LSP mean, LSP standard deviation.
2	LSP mean, Gray entropy, LBP uniformity, LSP standard deviation, Gray smoothness, Gray third moment, LSP third moment, LSP entropy, LSP uniformity, LBP mean, Gray uniformity, Gray standard deviation, GLCM homogeneity, LSP smoothness.
3	LBP smoothness, LBP uniformity, LBP third moment.
'Valencia' dataset	
1	Gray mean, Gray standard deviation, GLCM uniformity, Gray third moment, GLCM inertia, Gray smoothness, GLCM mean, GLCM homogeneity, LSP third moment, Gray entropy, Gray uniformity, GLCM cluster shade, GLCM maximum probability.
2	Gray entropy, Gray maximum probability.
3	Gray uniformity, Gray maximum probability, GLCM cluster shade, GLCM cluster prominence, LSP standard deviation, GLCM variance.
4	LSP uniformity, LBP mean, GLCM uniformity, LBP standard deviation.

Table 7. Number of samples in the 'Hamlin' dataset classified into each of four classes, classification accuracies, and misclassification errors.

	Actual Class				
Prediction	Healthy	HLB-Symptomatic	Zinc-Deficient HLB-Negative	Zinc-Deficient HLB-Positive	Sum
Healthy	**32 (100%)**	2 (7.1%)	0	0	34
HLB-symptomatic	0	**24 (85.7%)**	1 (6.7%)	0	25
Zinc-deficient, HLB-negative	0	0	**14 (93.3%)**	3 (20%)	17
Zinc-deficient, HLB-positive	0	2 (7.1%)	0	**12 (80%)**	14
Sum	32	28	15	15	90

Table 8. Number of samples in the 'Valencia' dataset classified into each of five classes, classification accuracies, and misclassification errors.

	Actual Class					
Prediction	Healthy	HLB-Symptomatic	Magnesium-Deficient	Zinc-Deficient HLB-Negative	Zinc-Deficient HLB-Positive	Sum
Healthy	**20 (100.0%)**	0	0	0	0	20
HLB-symptomatic	0	**20 (100.0%)**	1 (5.0%)	1 (16.7%)	3 (10.0%)	25
Magnesium-deficient	0	0	**19 (95.0%)**	0	0	19
Zinc-deficient HLB-negative	0	0	0	**2 (33.3%)**	5 (16.7%)	7
Zinc-deficient HLB-positive	0	0	0	3 (50.0%)	**22 (73.3%)**	25
Sum	20	20	20	6	30	96

datasets, respectively. The number of samples classified into the correct classes and their classification accuracies (in parentheses) are shown in the principal diagonal of the table, and the number of incorrect detections in each class and their misclassification errors (in parentheses) are shown in the other grids. Healthy samples were classified with 100% of accuracy in both datasets. The classification rates for HLB-symptomatic samples were 100% for the 'Valencia' dataset and 85.7% for the 'Hamlin' dataset. However, two out of four misclassified HLB-symptomatic samples in the 'Hamlin' dataset were identified as zinc-deficient HLB-positive, which means that their HLB infections were identified correctly. Only one magnesium-deficient sample in the 'Valencia' dataset was misclassified in the HLB-symptomatic class, which was a remarkable result because magnesium deficiency symptoms in citrus leaves are very similar to HLB symptoms. The classification rates in the zinc-deficient classes were usually lower than in the other classes because zinc deficiency symptoms hid the HLB symptoms in HLB-positive leaves.

Although the nutrient-deficient classes were included in the datasets, the main purpose of this study was to detect HLB infection and not nutrient deficiency. Therefore, the contents of tables 7 and 8 were merged into only two classes (HLB-positive and HLB-negative) for each dataset (table 9). Considering only HLB detection, average classification accuracies of 93.1% and 89.6% were achieved for the 'Hamlin' and 'Valencia' datasets, respectively.

Table 9. Number of samples classified into HLB-positive or HLB-negative classes, classification accuracies, and misclassification errors, regardless of nutrient deficiency condition, for the 'Hamlin' and 'Valencia' datasets.

	Actual Class		
Prediction	HLB-Positive	HLB-Negative	Sum
'Hamlin' dataset			
HLB-positive	**38 (88.4%)**	1 (2.1%)	39
HLB-negative	5 (11.6%)	**46 (97.9%)**	51
Sum	43	47	90
'Valencia' dataset			
HLB-positive	**45 (90.0%)**	5 (10.9%)	50
HLB-negative	5 (10.0%)	**41 (89.1%)**	46
Sum	50	46	96

DISCUSSION

This study investigated the effect of starch accumulation in HLB-symptomatic citrus leaves on the polarization planar of light at two specific wavelengths and employed it to develop a machine vision based sensing system that was able to distinguish between HLB-symptomatic and healthy leaves.

Generally, the starch concentration of healthy sweet orange leaf samples should not exceed 5 to 7 µg mm^{-2}; however, the 'Hamlin' dataset contained one healthy and eleven zinc-deficient HLB-negative samples with starch concentrations higher than 7 µg mm^{-2}. The starch concentrations in all six zinc-deficient HLB-negative samples of the 'Valencia' dataset also exceeded 7 µg mm^{-2}. This can be explained as either outliers or as HLB-symptomatic leaves not identified

by qrt-PCR analysis due to the many inconsistencies brought about by internal biotic conditions (Gottwald, 2010). However, the most reasonable explanation relates to the bacteria life cycle. Visible symptoms of starch accumulation (indicating high starch content) only arise after phloem plugging (Schneider, 1968; Etxeberria et al., 2009). During the process of phloem plugging and eventual collapse, CLas concentration declines, resulting in diminished DNA fingerprinting and lack of PCR detection (Folimonova and Achor, 2010). At some point, this situation results in CLas-infected leaves with high levels of starch but no positive PCR signal. The reverse situation was also found. One HLB-symptomatic sample and one zinc-deficient HLB-positive sample in the 'Hamlin' dataset, as well as four zinc-deficient HLB-positive samples in the 'Valencia' dataset, contained starch concentrations of less than 7 µg mm^{-2}, which could be considered an experimental error. However, the most reasonable explanation relates to the long latency period between HLB infection and the appearance of starch accumulation symptoms. In such cases, early HLB-infected leaves will give a positive PCR signal when the starch accumulation is in its early stages and has not yet reached the threshold level.

Our determination indicated that the 400 nm (Max), 400 nm (Min), and 591 nm (Max) images did not provide useful information for the detection process. The results obtained with 400 nm illumination confirmed the preliminarily results in which the reflectance ratio between healthy and HLB-symptomatic samples was close to one. The pixel values of the glossy regions of the 591 nm (Max) images were very similar to the pixel values of the HLB-symptomatic or zinc-deficient regions; as a result, the information in these images was impractical. As expected from the preliminarily results (fig. 1), the pixels belonging to healthy, HLB-symptomatic, and zinc-deficient regions in the 591 nm (Min) images were different (fig. 7), but the classification based on these pixel values did not always result in increased accuracy (fig. 7). One important reason for this discrepancy might be due to the AGC effect, which was not completely canceled in the calibration process. Leaf color inconsistency was also a minor reason for some samples. Consequently, a detection method based on image segmentation using a single threshold that can be applied to all leaf samples was not promising.

Most of the image textural descriptors, such as local pattern based textural features, are gray-scale invariant (Ojala et al., 1996), and the overall image brightness does not affect them. Hence, they were chosen for use in the detection process; as a result, the detection accuracy increased significantly. Local pattern features (LBP and LSP) included more than half of the features that were used for zinc deficiency detection and for HLB detection within the non-zinc-deficient class (table 5), as well as all three features that were used for HLB detection within the zinc-deficient class. Gray-scale invariant textural features such as entropy (which defines the busy-ness of an image) and smoothness and standard deviation (which depend on the image contrast) extracted directly from the images were also determined to be useful in zinc and HLB detection (table 6). It was concluded that the symptomatic areas of infected leaves generated different measures of image busy-ness and contrast compared to healthy leaves. The small contribution of GLCM features in all detection processes established that the pixels' spatial relationships in healthy and symptomatic samples were not noticeably different compared to the other textural descriptors. The Mahalanobis classifier resulted in the best accuracies in all classification steps for the 'Hamlin' dataset and in the first classification step for the 'Valencia' dataset.

The HLB detection accuracy within the zinc-deficient class was comparatively lower than in the non-zinc-deficient class for both datasets. This lower accuracy was expected because the zinc-deficient leaves already included some higher-intensity areas in the 591 nm (Min) images that were very similar to HLB-symptomatic areas but unrelated to HLB infection. Additionally, according to tables 3 and 4, the starch accumulations within the zinc-deficient classes (mostly in HLB-negative classes) were usually inconsistent with the corresponding PCR test results. This might be another reason for the lower classification rates in the zinc-deficient classes.

In total, five HLB-positive samples in each dataset were misclassified in the HLB-negative classes, which led to comparatively lower classification accuracies of 88.4%, and 90.0% for the HLB-positive classes in the 'Hamlin' and 'Valencia' datasets, respectively. Three of these five samples in the 'Hamlin' dataset and all five samples in the 'Valencia' dataset were within the zinc-deficient classes, and as explained before, HLB detection for zinc-deficient samples was less accurate. The measured starch concentrations for these samples were 2.63, 9.42, 12.49, 61.77, and 74.11 µg mm^{-2} in the 'Hamlin' dataset and 8.60, 10.69, 32.02, 47.12, and 51.53 µg mm^{-2} in the 'Valencia' dataset. One of these samples contained a starch concentration below the threshold (5 µg mm^{-2}), and the starch concentrations for five other samples were below the average for the HLB-symptomatic class (37.4 µg mm^{-2}). Therefore, the comparatively low concentration of starch might be a likely reason of misclassification. On the other hand, one HLB-negative sample in the 'Hamlin' dataset and five HLB-negative samples in the 'Valencia' dataset (all in nutrient-deficient classes) were misclassified into the HLB-positive classes. Although the CT values for these samples were "undetected" (which indicates that they were not infected), their starch concentration was 0.52, 8.0, 10.69, 11.13, 12.79, 20.90, and 40.30 µg mm^{-2}, which was above the threshold for five of them. Therefore, there is a possibility that the qrt-PCR analysis did not recognize their HLB infection, given the many stated inconsistencies outlined by Gottwald (2010), or their starch concentrations were elevated due to a different biological reason, a different disease, or a deficiency.

None of the confirmation methods, including crop scouting, starch measurement, and qrt-PCR analysis, are 100% accurate, and no absolute, precise detection approach has yet been reported. Consequently, the evaluation of the proposed method was certainly under the influence of this inaccuracy. Additionally, the incomplete gain adjustment process might be another source of error. Using a camera without an AGC feature may resolve this problem and increase the accuracy.

The results of this study demonstrate that starch accumulation due to HLB infection can be detected using polarizing filters with citrus leaf images taken at a wavelength of 591 nm. The starch accumulation in HLB-symptomatic leaves rotates the polarization planar of the light mostly around the 600 nm waveband, and a reflectance measurement system was capable of sensing this polarization rotation. However, this rotation was more clearly detected using textural features extracted from leaf images acquired with a commercial camera and proper use of polarizing filters. Using additional classes of nutrient-deficient samples that had visual symptoms similar to HLB infection verified that this system detected the starch accumulation in citrus leaves regardless of their visual color.

Laboratory-based detection methods, such as qrt-PCR analysis and starch measurement, may have higher accuracy; however, they are time consuming, labor intensive, and relatively expensive. Using spectroscopic approaches, Hawkins et al. (2010), Sankaran et al. (2011), and Pereira et al. (2011) achieved up to 95% of accuracy in HLB detection; however, their proposed methods required expensive equipment and trained staff. Li et al. (2013) showed that HLB detection accuracy could increase up to 86% using an improved airborne image analysis method; however, airborne imaging is not affordable by every grower, and the weather can limit its performance. In our study, an easy and inexpensive method was presented that can be used as a real-time, portable, in-field diagnostic tool with acceptable accuracy. Additionally, the unique characteristics in polarized light of the starch that accumulates in HLB-symptomatic leaves was used successfully for the first time in a real-time detection application.

CONCLUSION

In this study, an image acquisition system was developed to acquire citrus leaf images at 400 nm and 591 nm with polarized filters in parallel (maximum reflectance) and perpendicular (minimum reflectance) directions to the polarization planar of the light. It was determined that the images at 591 nm with minimum reflectance contained useful information for HLB detection. Using step-by-step classification models and different sets of textural features, overall HLB detection accuracies of 93.1%, 89.6% were obtained for the 'Hamlin' and 'Valencia' datasets, respectively. The results of this study demonstrate that the starch accumulation in HLB-symptomatic citrus leaves can be identified using the capability of starch to rotate the polarization planar of light. Considering that a simple, inexpensive imaging device in the visible range was used, and that there were two nutrient-deficient classes in the experiment, which made the detection more complicated, it can be concluded that this method can be used effectively in detecting HLB-positive leaves.

REFERENCES

Albrecht, U., & Bowman, K. D. (2008). Gene expression in Citrus sinensis (L.) osbeck following infection with the bacterial pathogen Candidatus Liberibacter asiaticus causing Huanglongbing in Florida. *Plant Sci., 175*(3), 291-306. http://dx.doi.org/10.1016/j.plantsci.2008.05.001.

Bishop, C. (2006). *Pattern recognition and machine learning* . New York, N.Y.: Springer.

Brown, C., Brown, M. G., Jauregui, C., Ferrell, L., Norberg, R. P., Barnhardt, V., & Griffith, T. (2011). *Citrus Reference Book.* Gainesville, Fla.: Florida Department of Citrus.

Choi, D., Lee, W. S., & Ehsani, R. (2013). Detecting and counting citrus fruit on the ground using machine vision. ASABE Paper No. 131591603. St. Joseph, Mich.: ASABE.

Etxeberria, E., Gonzalez, P., Achor, D., & Albrigo, G. (2009). Anatomical distribution of abnormally high levels of starch in HLB-affected Valencia orange trees. *Physiol. and Molec. Plant Path., 74*(1), 76-83. http://dx.doi.org/10.1016/j.pmpp.2009.09.004.

Folimonova, S. Y., & Achor, D. S. (2010). Early events of citrus greening (Huanglongbing) disease development at the ultrastructural level. *Phytopath., 100*(9), 949-958. http://dx.doi.org/10.1094/PHYTO-100-9-0949.

Gonzalez, P., Reyes-De-Corcuera, J., & Etxeberria, E. (2012). Characterization of leaf starch from HLB-affected and unaffected-girdled citrus trees. *Physiol. and Molec. Plant Path., 79*, 71-78. http://dx.doi.org/10.1016/ j.pmpp.2012.05.002.

Gottwald, T. R. (2010). Current epidemiological understanding of citrus Huanglongbing. *Ann. Rev. Phytopath., 48*, 119-139. http://dx.doi.org/10.1146/annurev-phyto-073009-114418.

Hawkins, S. A., Park, B., Poole, G. H., Gottwald, T., Windham, W. R., & Lawrence, K. C. (2010). Detection of citrus Huanglongbing by Fourier transform infrared-attenuated total reflection spectroscopy. *Applied Spectros., 64*(1), 100-103. http://dx.doi.org/10.1366/000370210790572043.

Huang, H.-L., & Chang, F.-L. (2007). ESVM: Evolutionary support vector machine for automatic feature selection and classification of microarray data. *Biosystems, 90*(2), 516-528. http://dx.doi.org/10.1016/j.biosystems.2006.12.003.

Kim, D. G., Burks, T. F., Schumann, A. W., Zekri, M., Zhao, X., & Jianwei, Q. (2009). Detection of citrus greening using microscopic imaging. *Agric. Eng. Intl. (CIGR Ejournal), 9*, manuscript 1194.

Li, H., Lee, W. S., Wang, K., Ehsani, R., & Yang, C. (2013). Extended spectral angle mapping (ESAM) for citrus greening disease detection using airborne hyperspectral imaging. *Precision Agric.* (on-line). http://dx.doi.org/10.1007/s11119-013-9325-6.

Li, H., Lee, W. S., Wang, R., Ehsani, R., & Yang, C. (2012a). Spectral angle mapper (SAM) based citrus greening disease detection using airborne hyperspectral imaging. *Proc. 11th Intl Conf. on Precision Agriculture.* Monticello, Ill.: International Society of Precision Agriculture.

Li, W., Hartung, J. S., & Levy, L. (2006). Quantitative real-time PCR for detection and identification of Candidatus Liberibacter species associated with citrus huanglongbing. *J. Microbiol. Methods, 66*(1), 104-115. http://dx.doi.org/10.1016/j.mimet.2005.10.018.

.

Li, X., Lee, W. S., Li, M., Ehsani, R., Mishra, A. R., Yang, C., & Mangan, R. L. (2012b). Spectral difference analysis and airborne imaging classification for citrus greening infected trees. *Computers and Electronics in Agric., 83*, 32-46. http://dx.doi.org/10.1016/j.compag.2012.01.010.

Li, X., Lee, W. S., Li, M., Ehsani, R., Mishra, A. R., Yang, C., & Mangan, R. L. (2011). Comparison of different detection methods for citrus greening disease based on airborne multispectral and hyperspectral imagery.ASABE Paper No. 1110570. St. Joseph, Mich.: ASABE.

Majumdar, S., & Jayas, D. S. (1999). Classification of bulk samples of cereal grains using machine vision. *J. Agric. Eng. Res., 73*(1), 35-47. http://dx.doi.org/10.1006/ jaer.1998.0388.

McMahon, K. A. (2004). Practical botany: The Maltese cross. In *Tested Studies for Laboratory Teaching* (Vol. 25, pp. 352-357). Association for Biology Laboratory Education.

Mishra, A., Ehsani, R., Albrigo, G., & Lee, W. S. (2007). Spectral characteristics of citrus greening (Huanglongbing). ASABE Paper No. 073056. St. Joseph, Mich.: ASABE.

Mishra, A., Karimi, D., Ehsani, R., & Albrigo, L. G. (2011). Evaluation of an active optical sensor for detection of Huanglongbing (HLB) disease. *Biosystems Eng., 110*, 302-309. http://dx.doi.org/10.1016/j.biosystemseng.2011.09.003.

Mishra, A. R., Karimi, D., Ehsani, R., & Lee, W. S. (2012). Identification of citrus greening (HLB) using a VIS-NIR spectroscopy technique. *Trans. ASABE, 55*(2), 711-720. http://dx.doi.org/10.13031/2013.41369.

Ojala, T. Pietikäinen, M., & Harwood, D. (1996). A comparative study of texture measures with classification based on featured distributions. *Pattern Recognition, 29*(1), 51-59. http://dx.doi.org/10.1016/0031-3203(95)00067-4.

Pereira, F. M. V., Milori, D. M. B. P., Pereira-Filho, E. R., Venínico, A. L., Russo, M. d. S. T., Cardinali, M. C. d. B., Martins, P. K., & Freitas-Astúa, J. (2011). Laser-induced fluorescence imaging method to monitor citrus greening disease. *Computers and Electronics in Agric., 79*, 90-93. http://dx.doi.org/10.1016/ j.compag.2011.08.002.

Pourreza, A., Lee, W. S., Raveh, E., Hong, Y., & Kim, H.-J. 2013. Identification of citrus greening disease using a visible-band image analysis. ASABE Paper No. 131591910. St. Joseph, Mich.: ASABE.

Pourreza, A., Pourreza, H., Abbaspour-Fard, M.-H., & Sadrnia, H. (2012). Identification of nine Iranian wheat seed varieties by textural analysis with image processing. *Computers and Electronics in Agric., 83*, 102-108. http://dx.doi.org/10.1016/ j.compag.2012.02.005.

Pourreza, H. R., Masoudifar, M., & ManafZade, M. (2011). LSP: Local similarity pattern, a new approach for rotation invariant noisy texture analysis. In *18th IEEE Intl. Conf. Image Processing (ICIP)* (pp. 837-840). Piscataway, N.J.: IEEE.

Putnam, A. H. (2012). *Florida agriculture: By the numbers.* Tallahassee, Fla.: Florida Department of Agriculture and Consumer Services.

Sankaran, S., & Ehsani, R. (2011). Visible-near infrared spectroscopy based citrus greening detection: Evaluation of spectral feature extraction techniques. *Crop Prot., 30*(11), 1508-1513. http://dx.doi.org/10.1016/j.cropro.2011.07.005.

Sankaran, S., Ehsani, R., & Etxeberria, E. (2010b). Mid-infrared spectroscopy for detection of Huanglongbing (greening) in citrus leaves. *Talanta, 83*, 574-581. http://dx.doi.org/10.1016/ j.talanta.2010.10.008.

Sankaran, S., Mishra, A., Ehsani, R., & Davis, C. (2010a). A review of advanced techniques for detecting plant diseaseS. *Computers and Electronics in Agric., 72*(1), 1-13. http://dx.doi.org/10.1016/ j.compag.2010.02.007.

Sankaran, S., Mishra, A., Maja, J. M., & Ehsani, R. (2011). Visible-near infrared spectroscopy for detection of Huanglongbing in citrus orchards. *Computers and Electronics in Agric., 77*(2), 127-134. http://dx.doi.org/10.1016/j.compag.2011.03.004.

Schneider, H. (1968). Anatomy of greening-disease sweet orange shots. *Phytopath., 58*, 1155-1160.

Xuan, G., Chai, P., & Wu, M. (1996). Bhattacharyya distance feature selection. In *Proc. 13th Intl. Conf. on Pattern Recognition* (pp. 195-199). Piscataway, N.J.: IEEE. http://dx.doi.org/10.1109/ICPR.1996.546751.